Development/Plasticity/Repair

Endogenous Tagging Reveals Differential Regulation of Ca²⁺ Channels at Single Active Zones during Presynaptic Homeostatic Potentiation and Depression

Scott J. Gratz,[1,2] Pragya Goel,[3] Joseph J. Bruckner,[4] Roberto X. Hernandez,[5] Karam Khateeb,[6] Gregory T. Macleod,[5] Dion Dickman,[3] and Kate M. O'Connor-Giles[1,2]

[1]Department of Neuroscience, [2]Carney Institute for Brain Science, Brown University, Providence, Rhode Island 02912, [3]Department of Neurobiology, University of Southern California, Los Angeles, California 90089, [4]Laboratory of Cell and Molecular Biology, University of Wisconsin-Madison, Madison, WI 53706, [5]Department of Biological Sciences and Wilkes Honors College, Florida Atlantic University, Jupiter, Florida 33458, and [6]Laboratory of Genetics, University of Wisconsin-Madison, Madison, WI 53706

Neurons communicate through Ca²⁺-dependent neurotransmitter release at presynaptic active zones (AZs). Neurotransmitter release properties play a key role in defining information flow in circuits and are tuned during multiple forms of plasticity. Despite their central role in determining neurotransmitter release properties, little is known about how Ca²⁺ channel levels are modulated to calibrate synaptic function. We used CRISPR to tag the *Drosophila* Ca$_V$2 Ca²⁺ channel Cacophony (Cac) and, in males in which all Cac channels are tagged, investigated the regulation of endogenous Ca²⁺ channels during homeostatic plasticity. We found that heterogeneously distributed Cac is highly predictive of neurotransmitter release probability at individual AZs and differentially regulated during opposing forms of presynaptic homeostatic plasticity. Specifically, AZ Cac levels are increased during chronic and acute presynaptic homeostatic potentiation (PHP), and live imaging during acute expression of PHP reveals proportional Ca²⁺ channel accumulation across heterogeneous AZs. In contrast, endogenous Cac levels do not change during presynaptic homeostatic depression (PHD), implying that the reported reduction in Ca²⁺ influx during PHD is achieved through functional adaptions to pre-existing Ca²⁺ channels. Thus, distinct mechanisms bidirectionally modulate presynaptic Ca²⁺ levels to maintain stable synaptic strength in response to diverse challenges, with Ca²⁺ channel abundance providing a rapidly tunable substrate for potentiating neurotransmitter release over both acute and chronic timescales.

Key words: synapse; calcium channels; *Drosophila*; gene editing; homeostatic plasticity; neurotransmitter release

Significance Statement

Presynaptic Ca²⁺ dynamics play an important role in establishing neurotransmitter release properties. Presynaptic Ca²⁺ influx is modulated during multiple forms of homeostatic plasticity at *Drosophila* neuromuscular junctions to stabilize synaptic communication. However, it remains unclear how this dynamic regulation is achieved. We used CRISPR gene editing to endogenously tag the sole *Drosophila* Ca²⁺ channel responsible for synchronized neurotransmitter release, and found that channel abundance is regulated during homeostatic potentiation, but not homeostatic depression. Through live imaging experiments during the adaptation to acute homeostatic challenge, we visualize the accumulation of endogenous Ca²⁺ channels at individual active zones within 10 min. We propose that differential regulation of Ca²⁺ channels confers broad capacity for tuning neurotransmitter release properties to maintain neural communication.

Introduction

Dynamic changes in the properties controlling neurotransmitter release at individual synaptic connections modulate information flow in neural circuits. Neurotransmitter release occurs at spe-cialized domains called active zones (AZs) where synaptic vesicles fuse to presynaptic membranes and release their contents following action potential-driven influx of Ca²⁺. AZ release properties are determined locally and can vary considerably within and be-

tween neuronal subtypes (Hatt and Smith, 1976; Atwood and Karunanithi, 2002; Branco and Staras, 2009; Südhof, 2012). However, how this remarkable diversity in AZ release properties is established, maintained, and dynamically adjusted during various forms of plasticity is poorly understood.

Synaptic vesicle release is a stochastic process that is subject to dynamic modulation over both acute and chronic timescales. The probability that an action potential will elicit fusion of a synaptic vesicle at a particular AZ (synaptic probability of release; P_r) is a defining property of neurotransmitter release that can be tuned during plasticity. Two key parameters have a large influence on P_r: the number of synaptic vesicles available for release and their individual probability of release. Vesicular release probability is heavily influenced by Ca²⁺ influx through presynaptic Ca²⁺ channels, which in turn is driven by the number, organization, and intrinsic properties of Ca²⁺ channels at AZs (Ariel and Ryan, 2012; Ehmann et al., 2015; Dittrich et al., 2018).

The *Drosophila* neuromuscular junction (NMJ) provides a powerful model for investigating the establishment and modulation of release properties at individual AZs *in vivo*. At fly NMJs, single *Drosophila* glutamatergic motorneurons form hundreds of synapses with their postsynaptic muscle targets. These presynaptic motor terminals have many parallels to excitatory synapses in the mammalian CNS, including molecular composition, AZ ultrastructural organization, and neurotransmitter release properties (Ackermann et al., 2015; Harris and Littleton, 2015; Zhan et al., 2016; Van Vactor and Sigrist, 2017). Further, functional imaging studies with genetically encoded Ca²⁺ indicators have facilitated the investigation of neurotransmission at single synapses of *Drosophila* motorneurons, revealing a remarkable degree of heterogeneity in release properties between individual AZs (Guerrero et al., 2005; Peled and Isacoff, 2011; Melom et al., 2013; Peled et al., 2014; Akbergenova et al., 2018). Finally, conserved forms of homeostatic plasticity are expressed at the *Drosophila* NMJ. In a process known as presynaptic homeostatic potentiation (PHP), genetic or pharmacological disruption of postsynaptic glutamate receptors induces a compensatory increase in neurotransmitter release that maintains overall synaptic strength (Frank, 2014; Davis and Müller, 2015). An opposing form of homeostatic plasticity, called presynaptic homeostatic depression (PHD), is observed in response to excess glutamate released from individual synaptic vesicles. In this paradigm, a homeostatic decrease in the number of vesicles released stabilizes synaptic strength (Daniels et al., 2004). Although the two forms of homeostatic plasticity rely on inverse modulations to Ca²⁺ influx through presynaptic Ca²⁺ channels (Müller and Davis, 2012; Gavino et al., 2015), the mechanisms that achieve these adaptations are unclear.

Here, we engineered the endogenous locus of *Drosophila cacophony* (*Cac*) to incorporate a fluorescent tag in all 15 known isoforms of Cac. Cac is the pore-forming subunit of the sole Ca²⁺ channel required for triggering synchronous neurotransmitter release in *Drosophila* (Smith et al., 1996; Kawasaki et al., 2000; Macleod et al., 2006; Peng and Wu, 2007). The generation of endogenously tagged Cac allowed us to probe the relationship between Ca²⁺ channel levels, P_r, and homeostatic plasticity. We found that the abundance of endogenous Cac is modulated during PHP, but does not change during PHD, indicating that distinct mechanisms are used to bidirectionally tune Ca²⁺ influx during these opposing forms of homeostatic plasticity. Live imaging of Cac at identified synapses before and after acute pharmacological induction of PHP revealed the proportional accumulation of Ca²⁺ channels across AZs, a mechanism that maintains the heterogeneous distribution of Ca²⁺ channels. We propose that differential regulation of Ca²⁺ channels at single AZs confers reliable neurotransmission and a broad capacity for tuning neurotransmitter release probability to maintain neural communication.

Materials and Methods

Drosophila genetics and genome engineering. The following fly lines are available at the Bloomington *Drosophila* Stock Center (BDSC): w^{1118} (RRID:BDSC_5905), *vasa-Cas9* (RRID:BDSC_51324), piggyBac transposase (RRID:BDSC_8283), and OK371-Gal4 (RRID:BDSC_26160; Horn et al., 2003; Parks et al., 2004; Gratz et al., 2014). The null allele *GluRIIA*^{SP16} (Petersen et al., 1997) and *UAS-vGlut* (Daniels et al., 2004) were generously provided by Aaron DiAntonio (Washington University School of Medicine). PS-GCaMP comprises an MHC promoter for muscle expression, an N-terminal myristoylation sequence for membrane targeting, GCaMP5, and the Shaker PDZ domain for targeting to the postsynaptic density, and was incorporated into the attP2 landing site (RRID:BDSC_25710). Endogenously tagged Cac was generated using a scarless CRISPR/piggyBac-based approach (flyCRISPR.molbio.wisc. edu; Bruckner et al., 2017). Briefly, sequences coding for sfGFP or TagRFP-T flanked by flexible linkers and a visible marker flanked by piggyBac inverted terminal repeat sequences were inserted immediately downstream of the second annotated translational start site of the endogenous *Cac* locus (base pairs 11,980,057 through 11,980,055, *D. melanogaster* genome release 6). This site is in an exon common to all isoforms of *Cac*. piggyBac transposase was subsequently used for footprint-free removal of the marker, followed by molecular confirmation of precise tag incorporation.

Presynaptic Ca²⁺ imaging and analysis. Ca²⁺ levels at motor terminals was measured by forward filling of dextran-conjugated indicators (Macleod, 2012). Male third instar larvae were dissected in chilled Schneider's insect medium (Sigma-Aldrich). Severed segmental nerves were drawn into a filling pipette, and a 16:1 mixture of the Ca²⁺ indicator rhod dextran (R34676; ThermoFisher Scientific) and a Ca²⁺-insensitive AlexaFluor 647 dextran (AF647 dextran; D22914; ThermoFisher Scientific) was applied to the cut nerve end for 15–45 min. Preparations were incubated in the dark for at least 3 h and rinsed every 30 min with fresh Schneider's insect medium. Thirty minutes before imaging, the Schneider's insect medium was replaced with hemolymph-like solution (HL6) containing 2.0 mM Ca²⁺ and supplemented with 7 mM L-glutamic acid (Macleod et al., 2002). Analysis was performed on type-Ib and type-Is motor neuron terminals innervating muscle 6 in hemisegment A3 or A4. Live imaging was performed on a Nikon Eclipse FN1 microscope with a 100× 1.1 NA water-immersion objective (Nikon) using an iXon3 888 EMCCD camera (Andor) operating at a frame rate of 114 Hz. The terminals were alternately excited at 550 ± 7 nm and 640 ± 15 nm, and emission was alternately collected at 605 ± 26 nm and 705 ± 36 nm, respectively. The cut end of the segmental nerve was stimulated using a 0.4 ms pulse 10 times at 1 Hz followed by a stimulus train at 20 Hz for 1 s. Images were background subtracted and analyzed by generating fluorescence intensity traces with NIS-Elements Ar (Nikon). For each preparation (N), 2–5 nonterminal boutons of a single NMJ were analyzed. Ca²⁺ levels are measured as the fluorescence ratio of rhod to AF647. Ten single

action potentials were averaged into a single trace and used to calculate peak amplitude and the decay time constant (tau). Ca^{2+} imaging data were excluded from further analysis if they were collected from terminals where resting Ca^{2+} levels were assessed to be outliers. The bounds used to assess outliers were calculated as follows: the median absolute deviation (MAD) was calculated for resting Ca^{2+} levels of each group of terminals and the upper boundary was defined as 3× MAD above the median, and the lower boundary was defined as 3× MAD below the median (Leys et al., 2013). No further criteria for exclusion of Ca^{2+} imaging data were applied, providing the fluorescence transient of the Ca^{2+} indicator recovered to the baseline with a time course of <250 ms (tau).

Electrophysiology. Male third instar larvae were dissected in modified Ca^{2+}-free hemolymph-like saline (HL3; in mM: 70 NaCl, 5 KCl, 10 MgCl$_2$, 10 NaHCO$_3$, 115 sucrose, 5 trehalose, 5 HEPES, pH 7.2; Stewart et al., 1994) as described previously (Kiragasi et al., 2017). Briefly, NMJ sharp electrode (electrode resistance between 10 and 30 MΩ) recordings were performed in HL3 saline containing 0.4 mM Ca^{2+} on muscles 6 and 7 of abdominal segments A2 and A3 using a sharp borosilicate electrode (resistance of 15–25 MΩ) filled with 3 M KCl. Recordings were performed on an Olympus BX61 WI microscope using a 40×/0.80 water-dipping objective, and acquired using an AxoClamp 900A amplifier, Digidata 1440A acquisition system, and pClamp 10.5 software (Molecular Devices). Electrophysiological sweeps were digitized at 10 kHz, and filtered at 1 kHz.

Miniature excitatory junctional potentials (mEJPs) were recorded in the absence of any stimulation, and cut motor axons were stimulated to elicit EJPs. For each recording, at least 100 mEJPs were analyzed using Mini Analysis (Synaptosoft) to obtain a mean mEJP amplitude value. EJPs were stimulated with an ISO-Flex stimulus isolator (AMPI), with intensity adjusted for each cell to consistently elicit responses from both type Ib and Is motorneurons innervating the muscle segment. At least 20 consecutive EJPs were recorded for each cell and analyzed in pClamp to obtain mean amplitude. Quantal content was determined for each recording by calculating the ratio of mean EJP amplitude to mean mEJP amplitude and then averaging recordings across all NMJs for a given genotype. Muscle input resistance (R_{in}) and resting membrane potential (V_{rest}) were monitored during each experiment. Recordings were analyzed only if the V_{rest} was between −60 and −80 mV and R_{in} was ≥5 MΩ.

Pharmacological homeostatic challenge was assessed by incubating semi-intact preparations in 20 μM Philanthotoxin-433 (PhTx; Santa Cruz Biotechnology, sc-255421, lot B1417) diluted in HL3 containing 0.4 mM Ca^{2+} for 10 min at room temperature (Frank et al., 2006). Following treatment, the dissection was completed and the prep was rinsed five times in recording solution. For analysis of Ca^{2+} channel levels following acute homeostatic plasticity, preparations were fixed in 4% PFA for 30 min following PhTx incubation and rinses, and stained as described below.

Immunostaining. Male third instar larvae were dissected in ice-cold Ca^{2+}-free saline and fixed for 30 min in 4% paraformaldehyde in PBS or 5 min in 100% ice-cold ethanol. Dissected larvae were washed and permeabilized in PBS containing 0.1% Triton-X and blocked for 1 h in 5% normal donkey serum or overnight at 4°C in PBS containing 0.1% Triton-X and 1% BSA. Dissected larvae were incubated in primary antibodies overnight at 4°C or 3 h at room temperature and secondary antibodies for 2–3 h at room temperature, then mounted in VECTASHIELD (Vector Laboratories) or ProLong Diamond (ThermoFisher Scientific). The following antibodies were used at the indicated concentrations: mouse anti-Bruchpilot (Brp) at 1:100 (DSHB, catalog #nc82; RRID: AB_2314866), rabbit anti-GFP conjugated to AlexaFluor 488 at 1:500 (ThermoFisher Scientific, catalog #A-21311; RRID:AB_221477), and anti-HRP conjugated to AlexaFluor 647 at 1:200–1:500 (Jackson ImmunoResearch). Species-specific Alexa Fluor 488 and 568 secondary antibodies (Invitrogen, Jackson ImmunoResearch) were used at 1:400–1:500.

Confocal imaging and analysis. Confocal images were acquired on a Nikon A1R-Si+ with Plan-Apo 60× 1.40 NA and 100× APO 1.4 NA oil-immersion objectives or an Olympus FluoView FV1000 with Plan-Apo 60× (1.42 NA) oil-immersion objective. Image analyses and bright-

ness and contrast adjustments were performed using the Fiji distribution of ImageJ (Schindelin et al., 2012). For analysis of Cac and Brp intensity, all genotypes were stained together and imaged in the same session with identical microscope settings optimized for detection without saturation of the signal. For consistency, analysis was limited to type Ib synapses of NMJ 6/7 in segments A2 and A3. Maximum intensity projections were used for quantitative image analysis using either NIS Elements software General Analysis toolkit or Fiji as follows. To measure Cac$^{sfGFP-N}$ and Brp intensity at individual AZs, nonsynaptic structures including axons were removed from the images using freehand selection and fill. Z-stacks were flattened using the Maximum Intensity Z-projection function. Channels were separated, background subtracted, and noise was reduced using a light Gaussian filter (0.75 pixel σ radius). A threshold was applied to the Brp channel to remove irrelevant low intensity pixels and individual puncta were identified and segmented using the Find Maxima tool. The resulting segmented Brp image was used to create a binary mask that was also used to segment the Cac$^{sfGFP-N}$ channel. Intensity data were collected using the Analyze Particles tool. The fluorescent intensity of each puncta is measured as the sum fluorescence calculated directly or as the product of average intensity and particle area.

Live imaging. Functional imaging experiments were performed using a Nikon A1R+ scanning confocal system built on a Nikon Eclipse FN1 microscope with a CFI Plan 100×W objective (Nikon). Cac$^{TagRFP-N}$; PS-GCaMP male third instar larvae were dissected in ice-cold Ca^{2+}-free HL3 and severed segmental nerves were drawn into a stimulating pipette. Preparations were then maintained in HL3 saline containing 1.5 mM Ca^{2+} and 25 mM Mg^{2+} for imaging. Type-Ib motor neuron terminals innervating muscle 6 in hemisegment A2 or A3 were first imaged using the galvanometer scanner to collect a Cac$^{TagRFP-N}$ Z-stack. GCaMP5 was then imaged continuously in a single focal plane using the resonant scanner with full frame averaging for a final acquisition rate of 15.3 frames/s. Evoked postsynaptic Ca^{2+} transients were stimulated by applying a 0.4 ms pulse every second. The stimulus amplitude was adjusted to reliably recruit the Ib input. 94–100 stimulations were recorded for each experiment. Cac$^{TagRFP-N}$ puncta location and intensity was analyzed in Fiji. Z-stacks were flattened using the Maximum Intensity Z-projection function. To identify individual Cac$^{TagRFP-N}$ puncta, a mask was created using a Gaussian filter (σ radius = 2) and unsharp mask (radius = 3, weight = 0.8). A threshold was then applied to the mask to remove lower intensity pixels between puncta and individual puncta were segmented using the Find Maxima tool. By identifying large puncta with two local intensity maxima, the Find Maxima tool facilitates the identification and segmentation of closely spaced AZs. From each resulting image, a binary mask was then created and used to isolate puncta in the original Z-projection. Each punctum was then interrogated for intensity and X-Y coordinates using the Analyze Particles tool. GCaMP movies were processed using Nikon Elements software. Motion artifacts during acquisition were corrected by aligning all frames to the first frame of the movie. Baseline fluorescence was subtracted from every frame using a frame created from the average of 10 nonstimulus frames that also lacked spontaneous release events, and noise was reduced using the Nikon Elements Advanced Denoising function. The X-Y coordinates of postsynaptic Ca^{2+} transients were collected from all stimulation frames manually or automatically, with the two approaches yielding concordant results. For manual analysis, X-Y coordinates were obtained using hand selection of individual fluorescence peaks. Only peaks that persisted and decayed over subsequent frames were recorded. For automated analysis, all stimulation frames were thresholded to remove background noise and the Find Maxima tool in Fiji was used to identify event X-Y coordinates. Each postsynaptic event was then assigned to a Cac$^{TagRFP-N}$ punctum through nearest neighbor analysis using Euclidean distance.

Live imaging of Cac$^{sfGFP-N}$ during acute PHP was performed on a Nikon A1R-HD scanning confocal system built on a Nikon Eclipse FN1 microscope with a CFI75 Apochromat 25× 1.1 NA objective (Nikon). Third instar larvae were minimally dissected in Ca^{2+}-free HL3 and one side of the body wall was carefully pinned down while avoiding any stretching of body wall muscles. Before treatment, Z-stacks of NMJ 6/7 were acquired using the resonant scanner with 4× averaging. Preparations were then exposed to 40 μM Philanthotoxin-433 (Santa Cruz Bio-

technology, sc-255421, lot F2018) or vehicle diluted in HL3 for 10 min. Because segmental nerves were left intact, experiments were performed in Ca²⁺-free HL3 to minimize muscle contractions and movement during imaging, a condition that does not affect PHP (Goel et al., 2017). Immediately following PhTx treatment, NMJs were reimaged using the same imaging parameters. To measure Cac$^{sfGFP-N}$ intensity at individual AZs, Z-stacks were flattened using the Maximum Intensity Z-projection function and background subtracted. A Gaussian filter (0.9 pixel σ radius) was applied to the after treatment images to aid in AZ recognition and masking. After images were then segmented using freehand selection and fill to remove nonsynaptic structures. A threshold was applied to remove irrelevant low intensity pixels and individual AZ puncta were identified and segmented using the Find Maxima tool. The resulting segmented image was used to create a binary mask to segment the unfiltered before- and after-treatment background-subtracted maximum intensity projections. Intensity data were collected using the Analyze Particles tool and post-PhTx intensities were corrected for vehicle-only effects. For consistency, analysis was restricted to type-Ib AZs of NMJ 6/7.

Experimental design and statistical analysis. Statistical analyses were conducted in GraphPad Prism 7, SigmaStat 3.5, and R. Single comparisons of normally distributed datasets, as determined by the D'Agostino–Pearson omnibus test, were conducted by Student's *t* test. Welch's correction was used in cases of unequal variance. The Mann–Whitney *U* test was used for single comparisons of non-normally distributed data. For multiple comparisons of normally distributed data, we performed ANOVA followed by Tukey's test. One-dimensional Pearson correlation coefficients (*r*) were used to compare intensity levels and release probability. Fisher's exact test was used to compare proportions. Paired *t* tests and Wilcoxon signed rank tests were used for comparison of normally and non-normally distributed repeated intensity measurements, respectively. Reported values are mean ± SEM unless otherwise stated. *P* values, statistical test used, and sample sizes are reported in each figure legend.

Results

Endogenous tagging of the Ca$_V$2 Ca²⁺ channel Cac

Cac is the only Ca$_V$2-family member in *Drosophila* and is homologous to mammalian N- and P/Q-type voltage-gated Ca²⁺ channels (Smith et al., 1996; Littleton and Ganetzky, 2000). Neurotransmitter release depends on the synaptic localization of Ca$_V$2 channels and mutations that impinge on their function are associated with significant neurophysiological dysfunction at synapses (Smith et al., 1998; Mochida, 2018; Nanou and Catterall, 2018). Investigation of synaptic Ca²⁺ channel levels and localization in *Drosophila* has relied on overexpression of a C-terminally tagged transgene using the GAL4/UAS system (Kawasaki et al., 2004). This approach has enabled the identification of multiple regulators of Ca²⁺ channel localization to AZs (Kittel et al., 2006; Graf et al., 2009, 2012; Liu et al., 2011; Müller et al., 2012; Bruckner et al., 2017). However, several aspects of this transgenic approach pose limitations for investigating the relationship between Ca²⁺ channels and synapse-specific release properties: (1) *cac* is necessarily overexpressed, generally at high levels, under the control of GAL4 instead of endogenous regulatory elements; (2) only 1 of 15 annotated *cac* transcripts (corresponding to isoform cac-RC) is expressed and is likely not subject to RNA editing, a conserved mechanism for regulating ion channel function observed in endogenous *cac* (3) the C-terminal position of GFP likely obstructs a conserved PDZ-binding domain that mediates known interactions with synaptic proteins; and (4) expression of the single *cac* isoform was shown to rescue viability, but not flight, in null alleles, indicating channel function is not fully restored and/or properly regulated (Kawasaki et al., 2002, 2004).

To overcome these limitations and establish a reagent for following all endogenous Ca$_V$2 channels *in vivo*, we targeted the translational start site of 14 of 15 annotated *cac* isoforms for incorporation of superfolder-GFP (sfGFP) using CRISPR-based gene editing (Fig. 1A). This insertion site also results in the in-frame translation of sfGFP within the longer N-terminal cytoplasmic domain of the single isoform (cac-RN) with an earlier start site, allowing us to follow the full complement of endogenously expressed Cac isoforms (Fig. 1B). *cac$^{sfGFP-N}$* flies are homozygous and hemizygous viable, emerge at expected frequencies, and are capable of effective flight. Cac$^{sfGFP-N}$ localizes to AZs marked by the AZ cytomatrix protein Brp at presynaptic terminals of larval motorneurons with remarkable specificity (Fig. 1C). Endogenous Cac also localizes to the synaptic neuropils of the larval ventral ganglion and adult brain (Fig. 1D,E). In the adult brain, it was immediately apparent that endogenous Cac levels vary between brain regions. Most notably, we consistently observe higher Cac levels in the mushroom body. Therefore, incorporation of a fluorescent tag at the endogenous locus of Cac reports the expected gross localization of Ca²⁺ channels in the *Drosophila* nervous system along with new insights without obvious defects in viability or behavior.

Normal synaptic function at *Cac$^{sfGFP-N}$* NMJs

To directly evaluate the function of endogenously tagged channels, we first assayed presynaptic Ca²⁺ levels via fluorescence imaging of a Ca²⁺-sensitive dye loaded into axon terminals *in situ* (Macleod, 2012). The use of a rapid-binding chemical dye loaded in fixed proportion to a Ca²⁺-insensitive dye provided ratiometric resolution of single action potential-mediated Ca²⁺ transients and allowed for direct comparisons between terminal types, preparations, and genotypes (Fig. 2A–E; Lu et al., 2016). The resting level of Ca²⁺ is no different between *cac$^{sfGFP-N}$* and wild-type larvae in either type-Ib (big) or -Is (small) terminals on muscle fiber 6 (Fig. 2C). Similarly, there is no indication of a deficit in single action potential-mediated Ca²⁺ influx in *cac$^{sfGFP-N}$* on the basis of 1 Hz stimuli-evoked fluorescence transients (Fig. 2D). Finally, we measured the amplitude of the Ca²⁺ plateau during trains of action potentials and did not detect a significant change in *cac$^{sfGFP-N}$* relative to wild type (Fig. 2E). Thus, although we cannot rule out the possibility that tag incorporation could have subtle effects on Ca²⁺ channel function, we observe normal Ca²⁺ levels at motor terminals. To further interrogate the impact of endogenous tagging, we investigated synaptic transmission at *cac$^{sfGFP-N}$* NMJs. Consistent with normal Ca²⁺ influx, this analysis revealed no differences between control and *cac$^{sfGFP-N}$* in mEJP frequency, mEJP amplitude, or quantal content (Fig. 2F–K).

In addition to its role in neurotransmission, Cac promotes synapse formation (Rieckhof et al., 2003). We assessed synaptic growth in *cac$^{sfGFP-N}$* animals and found a mild decrease in bouton number at NMJ6/7 (wild type, 130.2 ± 5.7, n = 42 NMJs from 12 larvae; *cac$^{sfGFP-N}$*, 113.5 ± 4.8, n = 48 NMJs from 13 larvae, p = 0.026, Student's *t* test). At NMJ4, there is no difference in bouton number between *cac$^{sfGFP-N}$* and wild type (wild type, 29.9 ± 1.0, n = 54 NMJs from 12 larvae; *cac$^{sfGFP-N}$*, 28.7 ± 1.3, n = 53 NMJs from 13 larvae, p = 0.15). Similarly, AZ number per bouton is unaltered at *cac$^{sfGFP-N}$* NMJs (wild type, 9.5 ± 0.26 AZs per bouton, n = 16 NMJs from 9 larvae; *cac$^{sfGFP-N}$*, 9.7 ± 0.28 AZs per bouton, n = 22 NMJs from 14 larvae, p = 0.67, Student's *t* test). These analyses indicate that the incorporation of a fluorescent tag into the endogenous protein does not substantively disrupt Cac function *in vivo*.
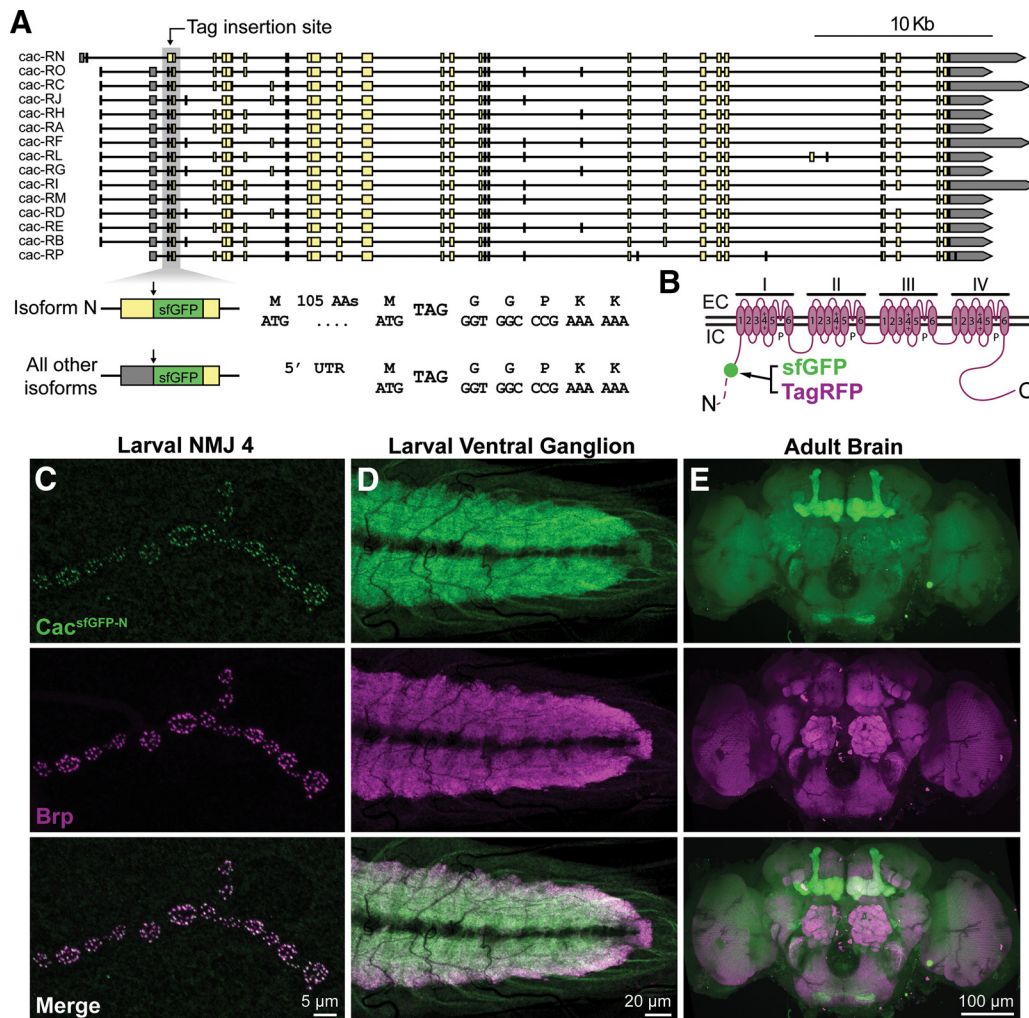
Figure 1. Endogenous tagging of the Ca$_v$2 Ca²⁺ channel Cacophony. **A**, Map of the *cacophony* locus indicating the genomic region targeted to incorporate sfGFP in all predicted isoforms. sfGFP is inserted between amino acids 107 and 108 of isoform cac-RN and immediately following the start codon in all other annotated isoforms. **B**, Schematic of the endogenously tagged Cac protein indicating the site of tag incorporation in the encoded channel (green dot). The longer N-terminus of the isoform encoded by cac-RN is represented by a dotted line. EC, Extracellular; IC, intracellular. **C–E**, Confocal Z-projections of a *cac*$^{sfGFP-N}$ larval NMJ (**C**), larval ventral ganglion (**D**), and adult brain (**E**) colabeled with antibodies against GFP and the active zone marker Brp.

Endogenous Cac levels are heterogeneous and correlate with P_r at single AZs

cac$^{sfGFP-N}$ allowed us to interrogate endogenous Ca²⁺ channel levels and their relationship to single AZ function at the hundreds of individual synapses formed between a single motorneuron and postsynaptic muscle cell. Using Brp puncta to delineate single AZs, we found that Cac intensity per AZ varies considerably within a single motorneuron terminal, with most AZs exhibiting low-to-moderate levels and a smaller number expressing high Cac levels (Fig. 3*A*,*B*). This broad dynamic range in Ca²⁺ channel abundance could, in principle, underlie a similarly broad range of Ca²⁺ influx and P_r at individual AZs. Indeed, functional imaging studies at *Drosophila* NMJs have revealed significant heterogeneity in P_r between individual synapses of motorneuron–muscle pairs with the majority of AZs exhibiting low P_r and a small minority exhibiting high P_r, similar to the distribution we observe for Ca²⁺ channel levels (Guerrero et al., 2005; Peled and Isacoff, 2011; Melom et al., 2013; Peled et al., 2014; Akbergenova et al., 2018). As Ca²⁺ channel levels would be predicted to correlate with single-AZ P_r and a recent study observed a positive correlation between exogenous Cac levels and P_r (Holderith et al., 2012; Sheng et al., 2012; Akbergenova et al., 2018), we next ex-

amined the relationship between endogenous Cac levels and synapse-specific neurotransmitter release properties at motor AZs. We replaced sfGFP in the endogenous *cac* locus with sequence encoding the slow-bleaching, monomeric red-shifted fluorophore TagRFP and confirmed the tag did not disrupt synaptic transmission (Fig. 2*F–K*). We then expressed postsynaptically targeted GCaMP5 (Akerboom et al., 2012) under the control of a muscle promoter (PS-GCaMP) in *cac*$^{TagRFP-N}$ flies and monitored neurotransmission via Ca²⁺ influx through postsynaptic glutamate receptors during 1 Hz stimulation. Using nearest neighbor analysis, we assigned each Ca²⁺ influx event to an AZ defined by the center of mass of each Cac$^{TagRFP-N}$-positive punctum and quantified the number of times a vesicle was released in response to 100 stimuli at individual AZs to calculate single-AZ P_r (Fig. 3*C*,*D*). We observed significant heterogeneity in release probability, with a positively skewed distribution that matches observations from previous studies (Peled and Isacoff, 2011; Melom et al., 2013; Peled et al., 2014). Specifically, we found that ~90% of AZs had release probabilities between 0.01 and 0.5, with a median P_r of 0.11, which corresponds remarkably well with physiological and prior optical imaging measurements (Lu et al., 2016; Newman et al., 2017).
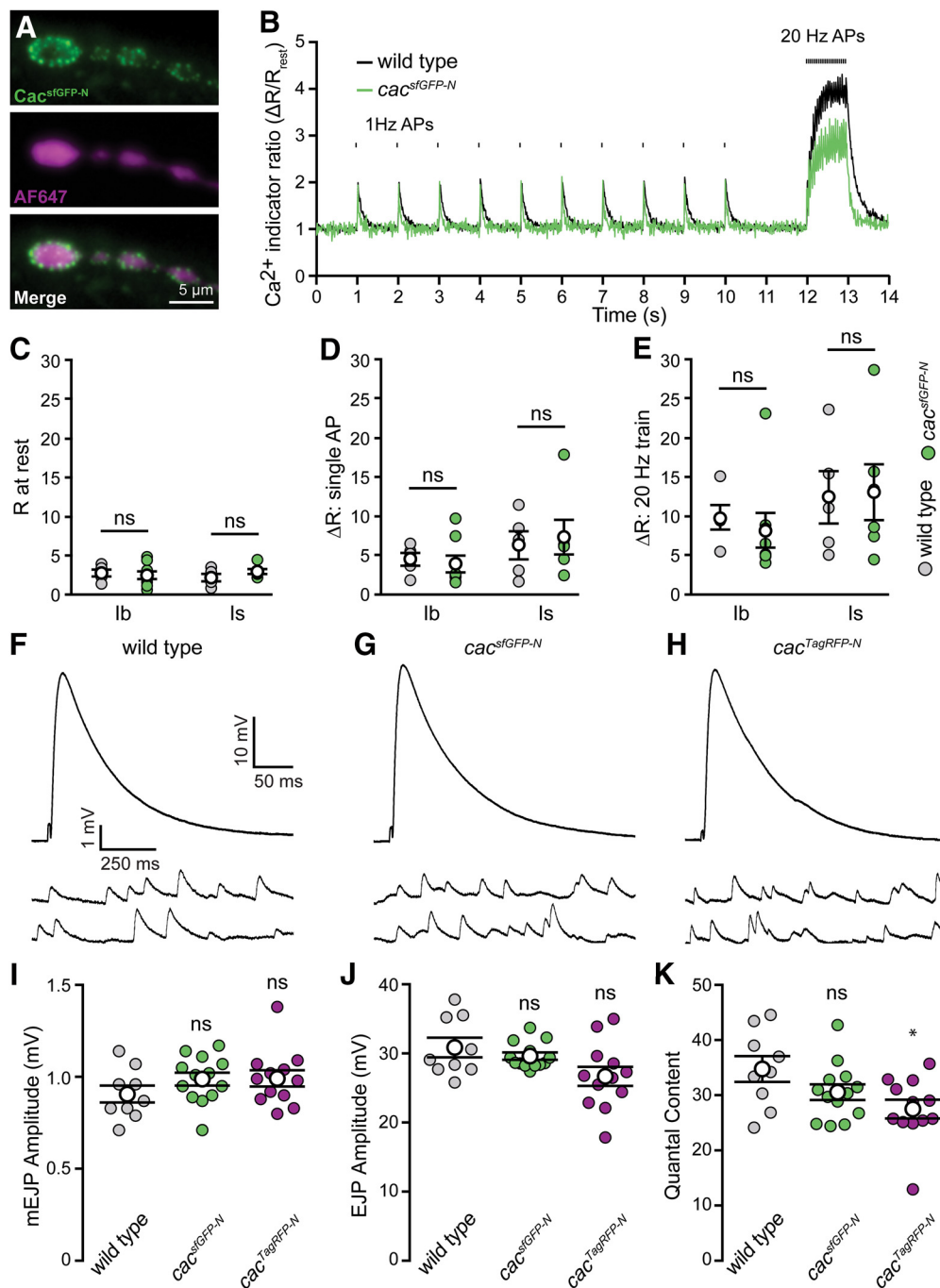
Figure 2. Endogenous tagging of Cacophony does not perturb presynaptic Ca²⁺ influx or synaptic function. ***A***, Live fluorescence images of type-Ib boutons from a $cac^{sfGFP-N}$ motor terminal showing Cac$^{sfGFP-N}$ (top) and AF647-dextran (center), which was co-loaded with rhod-dextran (image not shown). ***B***, Ratiometric fluorescence changes (rhod-dextran relative to AF647-dextran) in presynaptic motorneuron terminals during stimulation in wild type and $cac^{sfGFP-N}$. An action potential was initiated every second, for a period of 10 s, followed by a 1 s, 20 Hz train of action potentials. ***C***, Plot of average Ca²⁺ levels (R) in terminals before nerve stimulation for type-Ib and -Is terminals in wild-type and $cac^{sfGFP-N}$ boutons [wild-type Ib, 2.74 ± 0.44, one NMJ from each of 5 animals ($N = 5$); $cac^{sfGFP-N}$ Ib, 2.47 ± 0.49, $N = 8$, $p = 0.69$; wild-type Is, 2.16 ± 0.47, $N = 5$; $cac^{sfGFP-N}$ Is, 2.94 ± 0.32, $N = 6$, $p = 0.21$; Student's t test). ***D***, Plot of the average amplitude of single action potential-mediated Ca²⁺ transients [ΔR; wild-type Ib, 4.50 ± 0.81, one NMJ from each of 5 animals ($N = 5$); $cac^{sfGFP-N}$ Ib, 3.90 ± 1.07, $N = 8$, $p = 0.67$; wild-type Is, 6.28 ± 1.79, $N = 5$; $cac^{sfGFP-N}$ Is, 7.33 ± 2.20, $N = 6$, $p = 0.72$; Student's t test]. ***E***, Plot of the average amplitude of 1 s, 20 Hz action potential train-mediated Ca²⁺ transients [wild-type Ib, 9.71 ± 1.53, one NMJ from each of 5 animals ($N = 5$); $cac^{sfGFP-N}$ Ib, 8.13 ± 2.21, $N = 8$, $p = 0.57$; wild-type Is, 12.26 ± 3.36, $N = 5$; $cac^{sfGFP-N}$ Is, 12.94 ± 3.45, $N = 6$, $p = 0.89$; Student's t test]. ***F–H***, Representative traces of EJPs and mEJPs recorded in 0.4 mM Ca²⁺ at wild-type (***F***), $cac^{sfGFP-N}$ (***G***), and $cac^{TagRFP-N}$ NMJs (***H***). ***I***, mEJP amplitude is unaffected in $cac^{sfGFP-N}$ and $cac^{TagRFP-N}$ (wild type, 0.91 ± 0.05, $n = 9$ NMJs from 4 larvae; $cac^{sfGFP-N}$, 0.99 ± 0.04, $n = 13$ NMJs from 4 larvae, $p = 0.17$, Student's t test; $cac^{TagRFP-N}$, 0.99 ± 0.04, $n = 12$ NMJs from 4 larvae, $p = 0.20$, Mann–Whitney U test). ***J***, EJP amplitude is unchanged between wild-type, $cac^{sfGFP-N}$ and $cac^{TagRFP-N}$ NMJs (wild type, 30.87 ± 1.41, $n = 9$ NMJs from 4 larvae; $cac^{sfGFP-N}$, 29.64 ± 0.52, $n = 13$ NMJs from 4 larvae, $p = 0.84$, Mann–Whitney U test; $cac^{TagRFP-N}$, 26.70 ± 1.39, $n = 12$ NMJs from 4 larvae, $p = 0.05$, Student's t test). ***K***, Quantal content is similar between wild-type, $cac^{sfGFP-N}$ and $cac^{TagRFP-N}$ NMJs (wild type, 34.8 ± 2.3, $n = 9$ NMJs from 4 larvae; $cac^{sfGFP-N}$, 30.6 ± 1.4, $n = 13$ NMJs from 4 larvae, $p = 0.12$, Student's t test; $cac^{TagRFP-N}$, 27.5 ± 1.7, $n = 12$ NMJs from 4 larvae, $p = 0.03$, Mann–Whitney U test). Not significant (ns) and *$p < 0.05$.
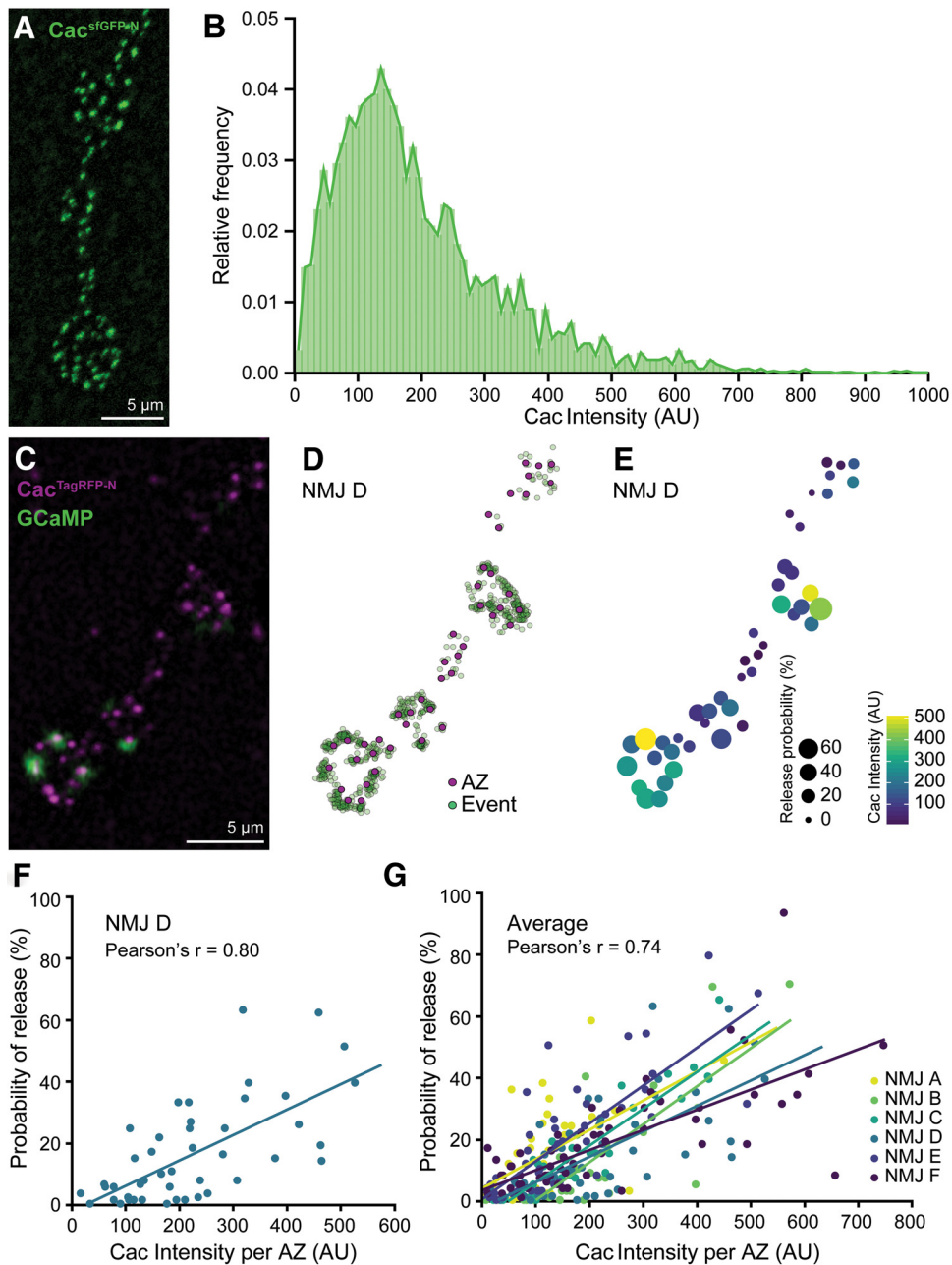
Figure 3. Cac $^{sfGFP-N}$ is heterogeneously distributed and highly correlated with P_r at individual AZs. **A**, Confocal Z-projection of a $cac^{sfGFP-N}$ NMJ labeled with an antibody against GFP. **B**, Broad distribution of Cac intensity across motorneuron AZs [$n = 3067$ AZs (10 data points are outside the x-axis limits shown) from 16 NMJs of 4 animals]. **C**, Confocal Z-projection of Cac $^{TagRFP-N}$ superimposed on a single frame of a PS-GCaMP movie monitoring neurotransmission in a live $cac^{TagRFP-N}$; PS-GCaMP preparation. **D**, Schematic of release events detected through postsynaptic GCaMP imaging (green dots) during 1 Hz stimulation mapped to individual AZs marked by Cac $^{TagRFP-N}$ (magenta dots). **E**, Heat map indicating P_r and Cac intensity at each AZ by spot size and color, respectively. **F**, Correlation between Cac and P_r at a single NMJ (NMJ D, shown in **C–E**; $r = 0.80$, $n = 44$ AZs). **G**, Correlation between Cac and P_r at six NMJs in six larvae (average $r = 0.74$).

When we compared P_r to Cac levels at individual AZs, we observed a strong positive correlation between Cac intensity and P_r as predicted (Fig. 3E–G). Consistent with the previous finding that Brp levels positively correlate with P_r (Muhammad et al., 2015; Reddy-Alla et al., 2017), we found that Cac and Brp levels are highly correlated ($r = 0.95$, $R^2 = 0.90$, $n = 2570$ AZs from 12 NMJs). This suggests that Brp levels largely predict Cac levels and that there is little additional predictive information in Brp measurements. However, this does not rule out the possibility that Brp levels also predict other parameters that influence P_r, such as readily releasable pool of synaptic vesicles (RRP) size, which

may be coordinately regulated with the AZ cytomatrix and Ca²⁺ channels. Finally, we considered the possibility that high-Cac, high-P_r AZs represented the combined molecular content and output of two adjacent AZs mistakenly identified as single AZs in our analysis. Our imaging parameters provided lateral resolution of ~250 nm, so more closely spaced AZs would not be resolved. A recent study used super-resolution microscopy to investigate the spacing between AZs and determined that fewer than 2.5% of *Drosophila* motor AZs are separated by less than 280 nm (Akbergenova et al., 2018), indicating that the majority of high-Cac, high-P_r AZs we ob-

serve are indeed single AZs. These data suggest the heterogeneity in Ca^{2+} channel levels is a key factor in establishing functional diversity between AZs of single neurons, and demonstrate that endogenously tagged Cac is a high-fidelity predictor of P_r.

Distinct regulation of Cac-sfGFP during the chronic expression of PHP and PHD

Multiple forms of adaptive plasticity modulate presynaptic release properties (Regehr, 2012; Kittel and Heckmann, 2016; Jackman and Regehr, 2017; Monday and Castillo, 2017; Van Vactor and Sigrist, 2017). PHP is a conserved mechanism for maintaining synaptic strength within a stable range (Cull-Candy et al., 1980; Frank, 2014; Davis and Müller, 2015). At the *Drosophila* NMJ, genetic perturbation of glutamate receptors triggers a retrograde signal that instructs presynaptic neurons to chronically increase neurotransmitter release to precisely offset the postsynaptic deficit (Petersen et al., 1997). In contrast, presynaptic overexpression of the vesicular glutamate transporter vGlut increases the amount of glutamate in each synaptic vesicle, triggering a decrease in the number of vesicles released per action potential to restore synaptic strength (Daniels et al., 2004). Prior studies showed that increases in Ca^{2+} influx and the RRP underlie PHP, whereas PHD is associated with decreased Ca^{2+} influx, but no change in the RRP (Weyhersmüller et al., 2011; Müller and Davis, 2012; Gavino et al., 2015; Kiragasi et al., 2017; Li et al., 2018a). Although modulation of Ca^{2+} influx contributes to the expression of both forms of homeostatic plasticity, the underlying mechanisms are not clear. In principle, presynaptic Ca^{2+} levels could be modulated through changes to the action potential waveform, Ca^{2+} buffering, Ca^{2+} channel gating properties, and/or Ca^{2+} channel abundance at AZs. A recent investigation ruled out changes to the action potential waveform during both PHP and PHD (Gavino et al., 2015). However, it was recently reported that transgenically overexpressed Cac-GFP levels were increased in *GluRIIA* mutants and decreased following overexpression of vGlut (Gavino et al., 2015; Li et al., 2018a), suggesting the simple model that bidirectional modulation of Ca^{2+} channel abundance drives opposing changes in Ca^{2+} influx during PHP and PHD. We tested this model using endogenously tagged Cac.

First, we confirmed that both PHP and PHD are expressed normally in *cac$^{sfGFP-N}$* animals through intracellular recordings (Fig. 4A–F). Next, we investigated Cac$^{sfGFP-N}$ levels in *GluRIIA* null mutants to determine whether endogenous Ca^{2+} channel levels are enhanced during chronic PHP expression. Consistent with the modulation of overexpressed Cac-GFP (Li et al., 2018a), we found that endogenous Ca^{2+} channel levels are indeed increased 36% in *GluRIIA* mutants (Fig. 4G–I). We also found that Brp levels were similarly increased (Fig. 4H,I); a change that was previously reported and postulated to underlie the observed increase in RRP size (Weyhersmüller et al., 2011; Goel et al., 2017; Li et al., 2018a). Thus, a coordinated accumulation of both Brp and Cac are observed during chronic PHP expression, consistent with these AZ components contributing to the homeostatic increase in Ca^{2+} influx and the RRP.

We next tested the model by investigating the modulation of endogenous Cac levels at NMJs overexpressing vGlut (VGlut-OE). In contrast to PHP, we did not observe a significant change in endogenous Ca^{2+} channel levels despite the robust expression of PHD (Fig. 4G,H,J). In agreement with Gavino et al. (2015), we also found no change in the abundance of the AZ cytomatrix protein Brp (Fig. 4G,H,J). To reconcile the difference between overexpressed and endogenous Cac, we repeated our analysis

with Gal4-driven UAS-Cac-GFP (Cac-OE). As previously reported, we observed robust PHD expression and a decrease in overexpressed Cac-GFP levels, most notably at AZs of type Is boutons where Gavino et al. (2015) observed the greatest reduction (Cac-OE: 1.0 ± 0.04, *n* = 15 NMJs; vGlut-OE; Cac-OE: 0.61 ± 0.03, *n* = 24 NMJs, *p* < 0.0001, Mann–Whitney *U* test). In contrast, we observed no change in endogenous Cac levels at AZs of type Is boutons overexpressing vGlut (*cac$^{sfGFP-N}$*, 1.0 ± 0.06, *n* = 15 NMJs; *cac$^{sfGFP-N}$*; vGlut-OE, 1.1 ± 0.06, *n* = 10 NMJs, *p* = 0.14, Mann–Whitney *U* test), similar to our observations at type Ib AZs (Fig. 4H). This points to the use of the transgenic construct as the source of the discrepancy and highlights potential differences between the regulation of exogenous versus endogenous ion channels. Together, these findings suggest that increased Cac abundance contributes to increased Ca^{2+} influx and P_r during chronic PHP adaptation, but that diminished Ca^{2+} influx during PHD is likely achieved through functional modulation of channel gating properties. More generally, these results indicate that AZ reorganization during PHP involves the coordinated recruitment of new vesicles to the RRP and an increase in Ca^{2+} channel levels, whereas PHD occurs without apparent morphological reorganization of the AZ, changes to RRP size, or modulation of Ca^{2+} channel levels, highlighting the diversity of responses used by AZs to maintain stable synaptic communication.

AZ Ca^{2+} channel levels are rapidly increased during adaptation to acute postsynaptic receptor perturbation

At the *Drosophila* NMJ, PHP can be acutely induced through pharmacological inhibition of postsynaptic GluRIIA-containing glutamate receptors by the wasp venom PhTx. This triggers a potentiation of neurotransmitter release that precisely offsets the postsynaptic deficit within 10 min (Frank et al., 2006). There is evidence that the pathways that mediate chronic and acute PHP are partially overlapping, and both involve increased Ca^{2+} influx, RRP size, and Brp levels (Frank et al., 2006; Weyhersmüller et al., 2011; Müller and Davis, 2012; Müller et al., 2012; Goel et al., 2017; Kiragasi et al., 2017). However, the regulation of Cac levels during acute PHP expression has not been investigated.

To determine whether endogenous Ca^{2+} channel levels are modulated over rapid timescales, we first assessed PhTx-induced PHP in *cac$^{sfGFP-N}$* larvae. As expected, we observe a robust homeostatic increase in neurotransmitter release (Fig. 5A–C). We then treated partially dissected *cac$^{sfGFP-N}$* larvae with nonsaturating concentrations of PhTx for 10 min and, immediately following PhTx treatment, fully dissected, fixed, and stained preparations for imaging of Cac and Brp. Strikingly, we observed a large increase in Cac levels (Fig. 5D–G). We also observed a significant increase in Brp levels across AZs (Fig. 5D–F,H) as previously reported (Weyhersmüller et al., 2011; Goel et al., 2017). Thus, Ca^{2+} channels accumulate at AZs within minutes during homeostatic potentiation of neurotransmitter release. Together with the prior finding that RRP levels increase on a similar timescale (Weyhersmüller et al., 2011), this indicates that AZs undergo a coordinated increase in size and molecular content during the acute expression of PHP, as they do over chronic timescales. Importantly, this finding does not rule out concurrent functional modulation of channels, but builds on prior findings to demonstrate that AZs are highly dynamic and capable of rapid growth that simultaneously increases not only the size of the RRP, but also Ca^{2+} channel levels.

We observe significant differences in baseline Cac levels and P_r between individual AZs of single motorneurons. Although the
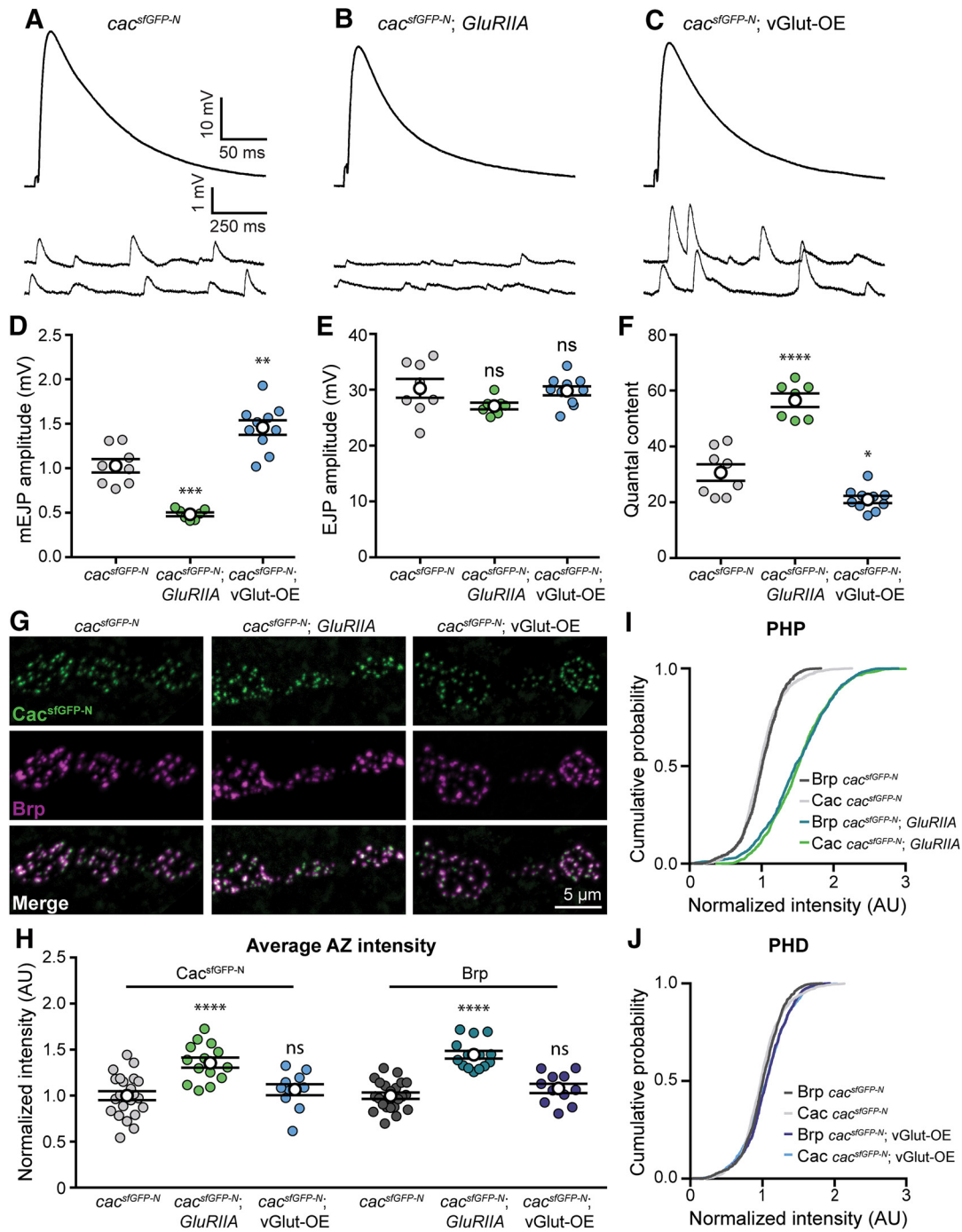
Figure 4. Endogenous Cac is differentially regulated in chronic PHP and PHD. **A–F**, Chronic expression of PHP and PHD occurs normally in $cac^{sfGFP-N}$ animals lacking GluRIIA ($GluRIIA^{SP16}$) or overexpressing vGlut (vGlut-OE; *OK371-Gal4>UAS-vGlut*), respectively. **A–C**, Representative traces of EJPs and mEJPs recorded in 0.4 mM Ca^{2+} at $cac^{sfGFP-N}$ (**A**), $cac^{sfGFP-N}$; *GluRIIA* NMJs (**B**), and $cac^{sfGFP-N}$; vGlut-OE (**C**). **D**, mEJP amplitude is decreased in $cac^{sfGFP-N}$; *GluRIIA* and increased in $cac^{sfGFP-N}$; vGlut-OE as expected ($cac^{sfGFP-N}$, 1.0 ± 0.08, $n = 8$ NMJs from 4 larvae; $cac^{sfGFP-N}$; *GluRIIA*, 0.48 ± 0.02, $n = 7$ NMJs from 4 larvae, $p = 0.0001$, t test with Welch's correction; $cac^{sfGFP-N}$; vGlut-OE, 1.5 ± 0.08, $n = 10$ NMJs from 4 larvae, $p = 0.0017$, Student's t test). **E**, EJP amplitude is unchanged between $cac^{sfGFP-N}$, $cac^{sfGFP-N}$; *GluRIIA* and $cac^{sfGFP-N}$; vGlut-OE NMJs ($cac^{sfGFP-N}$, 30.3 ± 1.70, $n = 8$ NMJs from 4 larvae; $cac^{sfGFP-N}$; *GluRIIA*, 27.1 ± 0.60, $n = 7$ NMJs from 5 larvae, $p = 0.1115$, t test with Welch's correction; $cac^{sfGFP-N}$; vGlut-OE, 29.8 ± 0.81, $n = 10$ NMJs from 4 larvae, $p = 0.80$, Student's t test), as expected. **F**, Quantal content is increased in $cac^{sfGFP-N}$; *GluRIIA* and decreased in $cac^{sfGFP-N}$; vGlut-OE as expected ($cac^{sfGFP-N}$, 30.7 ± 3.0, $n = 8$ NMJs from 4 larvae; $cac^{sfGFP-N}$; *GluRIIA*, 56.6 ± 2.4, $n = 7$ NMJs from 4 larvae, $p < 0.0001$, Student's t test; $cac^{sfGFP-N}$; vGlut-OE, 21.0 ± 1.3, $n = 10$ NMJs from 4 larvae, $p = 0.0145$, t test with Welch's correction). **G**, Confocal Z-projections of Cac and Brp in $cac^{sfGFP-N}$, in $cac^{sfGFP-N}$; *GluRIIA* and in $cac^{sfGFP-N}$; vGlut-OE motorneuron boutons colabeled with antibodies against GFP and Brp. **H**, Normalized intensity of Cac and Brp puncta averaged for each NMJ in control, *GluRIIA* and vGlut-OE animals (Cac levels: $cac^{sfGFP-N}$, 1.00 ± 0.05, $n = 22$ NMJs from 9 larvae; $cac^{sfGFP-N}$; *GluRIIA*, 1.36 ± 0.06, $n = 14$ NMJs from 5 larvae, $p < 0.0001$, Student's t test; and $cac^{sfGFP-N}$; vGlut-OE, 1.07 ± 0.06, $n = 11$ NMJs from 5 larvae, $p = 0.43$, Student's t test. Brp levels: $cac^{sfGFP-N}$, 1.00 ± 0.05, $n = 22$ NMJs from 4 larvae; $cac^{sfGFP-N}$; *GluRIIA*, 1.44 ± 0.04, $n = 14$ NMJs from 5 larvae, $p < 0.0001$, Student's t test; $cac^{sfGFP-N}$; vGlut-OE, 1.08 ± 0.06, $n = 11$ NMJs from 5 larvae, $p = 0.19$, Student's t test). **I**, Cumulative probability distributions of Cac and Brp puncta intensities demonstrate an increase in both Brp and Cac levels across AZs of *GluRIIA* animals [Cac levels: $cac^{sfGFP-N}$, $n = 1475$ AZs; $cac^{sfGFP-N}$; *GluRIIA*, $n = 1475$; (3 data points are outside the x-axis limits shown); Brp levels: $cac^{sfGFP-N}$, $n = 1475$ AZs; $cac^{sfGFP-N}$; *GluRIIA*, $n = 1475$ AZs]. **J**, Cumulative probability distributions of Cac and Brp puncta intensities show no decrease in Brp or Cac levels across AZs of vGlut-OE animals [Cac levels: $cac^{sfGFP-N}$, $n = 1475$ AZs; $cac^{sfGFP-N}$; vGlut-OE, $n = 1443$ (7 data points are outside the x-axis limits shown); Brp levels: $cac^{sfGFP-N}$, $n = 1475$ AZs; $cac^{sfGFP-N}$; vGlut-OE, $n = 1443$ AZs]. Not significant (ns), *$p < 0.05$, **$p < 0.01$, ***$p < 0.001$, and ****$p < 0.0001$.
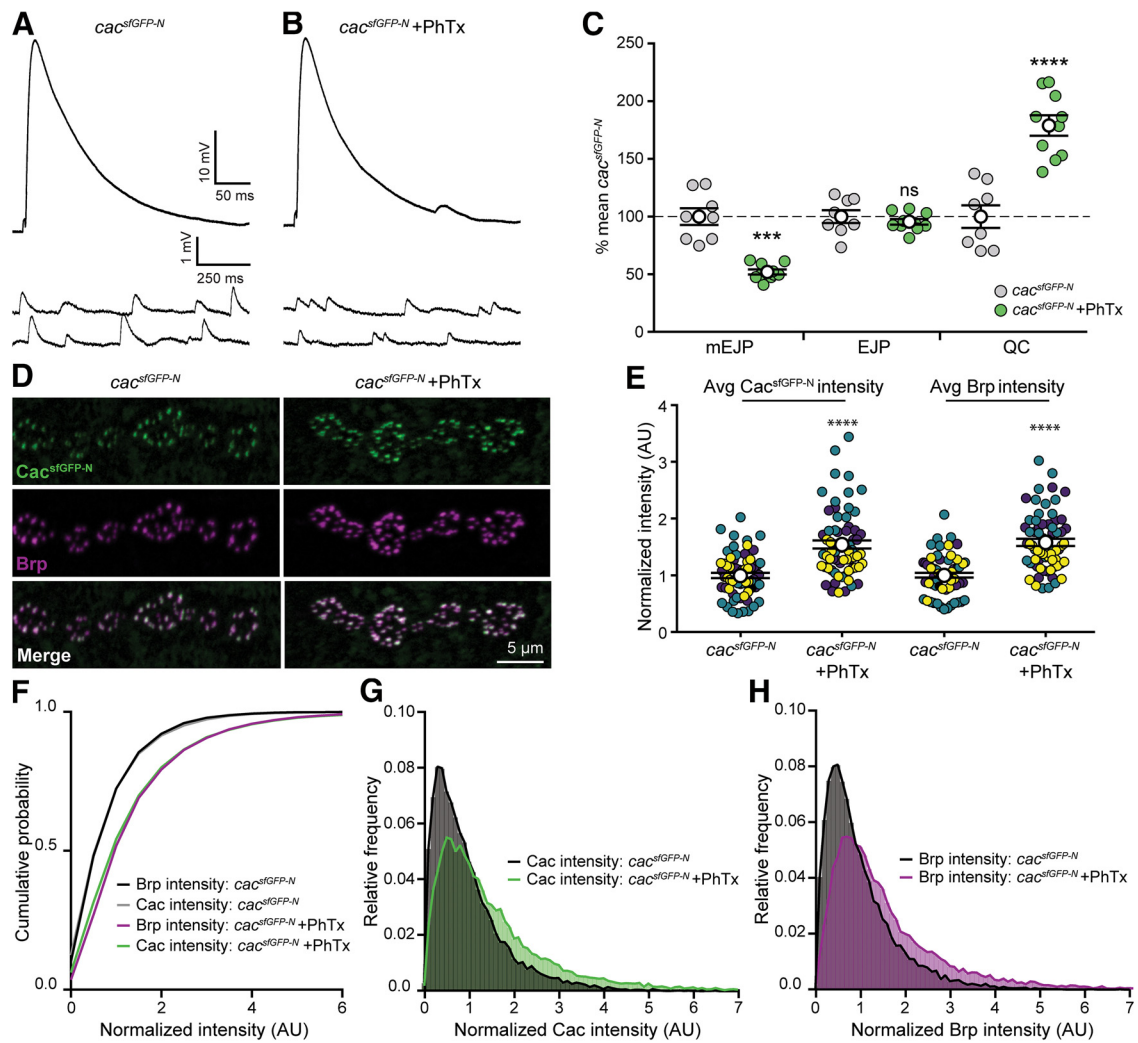
Figure 5. Cacophony levels are rapidly upregulated following acute homeostatic challenge. ***A***, ***B***, Representative traces of EJPs and mEJPs recorded at $cac^{sfGFP-N}$ NMJs in 0.4 mM Ca²⁺ with (***B***) or without (***A***) 10 min application of PhTx. ***C***, PhTx exposure significantly reduces mEJP amplitude at $cac^{sfGFP-N}$ NMJs ($cac^{sfGFP-N}$, 100 ± 7.3%, n = 8 NMJs from 4 larvae; $cac^{sfGFP-N}$ + PhTx, 52 ± 2.2%, n = 10 NMJs from 4 larvae, p = 0.0002, t test with Welch's correction) as expected. In response to PhTx exposure, EJP amplitude is maintained ($cac^{sfGFP-N}$, 100 ± 5.6%, n = 8 NMJs from 4 larvae; $cac^{sfGFP-N}$ + PhTx, 95.5 ± 2.5%, n = 10 NMJs from 4 larvae, p = 0.4393, Student's t test) as quantal content is significantly increased at $cac^{sfGFP-N}$ NMJs ($cac^{sfGFP-N}$, 100 ± 9.7%, n = 8 NMJs from 4 larvae; $cac^{sfGFP-N}$ + PhTx, 179.1 ± 8.8%, n = 10 NMJs from 4 larvae, p < 0.0001, Student's t test). ***D***, Confocal Z-projections of $cac^{sfGFP-N}$ motorneuron boutons colabeled with antibodies against GFP and Brp following vehicle (control) and PhTx treatment. ***E***, Normalized intensity of Cac and Brp per AZ averaged for each NMJ following 10 min vehicle or PhTx treatment from three independent experiments (yellow, green, and purple symbols) reveal a significant increase in both Brp and Cac levels immediately following PhTx treatment (Cac levels: control, 1.0 ± 0.05, n = 65 NMJs from 18 larvae; PhTx, 1.54 ± 0.07, n = 68 NMJs from 18 larvae, p < 0.0001, Mann–Whitney U test. Brp levels: control, 1.0 ± 0.04, n = 65 NMJs from 18 larvae; PhTx, 1.58 ± 0.06, n = 68 NMJs from 18 larvae, p < 0.0001, t test with Welch's correction). ***F***, Cumulative probability distributions of Cac and Brp intensities in control and PhTx-treated $cac^{sfGFP-N}$ animals [control, n = 13,908 AZs; PhTx, n = 15,925 AZs (80 data points are outside the x-axis limits shown)]. ***G***, ***H***, Frequency distributions of Cac and Brp intensities at individual AZs of control and PhTx-treated $cac^{sfGFP-N}$ animals reveal a rightward shift in intensities. Not significant (ns), ***p < 0.001, and ****p < 0.0001.

functional significance of this heterogeneity is unknown, it is clear that a small subset of AZs is responsible for the majority of neurotransmitter release under baseline conditions. PHP might similarly be achieved through the potentiation of a subset of AZs. Alternatively, potentiation may occur broadly across functionally heterogeneous AZs to scale release to an appropriate new level. We used live imaging of $cac^{sfGFP-N}$ to address this question by quantifying Cac levels at the same AZs before and after PhTx-induced PHP. We observed increased Cac levels at identified AZs 10 min after PhTx application (Fig. 6A). Paired analysis of single AZs demonstrated that Ca²⁺ channel levels were significantly increased relative to control across AZs with heterogeneous baseline states, although levels change little or decrease at a subset of AZs (Fig. 6 B, C). These findings are further supported by our fixed imaging results, where we observed a significant rightward

shift in the entire distributions of Cac and Brp following PhTx treatment (Fig. 5G,H). The smaller increase in Cac levels observed in our live imaging assays is likely due to the use of imaging conditions optimized for rapid acquisition and minimization of photobleaching. Given the heterogeneity in baseline Cac levels and P_r, we next investigated how the degree of Ca²⁺ channel accumulation might be influenced by the baseline state of an AZ. Cac content could be increased by addition of the same amount of Cac to all AZs (additive model; green) or by an amount proportional to baseline levels (multiplicative model; orange). We found that the data are well explained by a multiplicative model, indicating a proportional increase in Ca²⁺ channel levels across heterogeneous AZs (Fig. 6D). We next examined the population of AZs where Cac content is unchanged or decreased, and
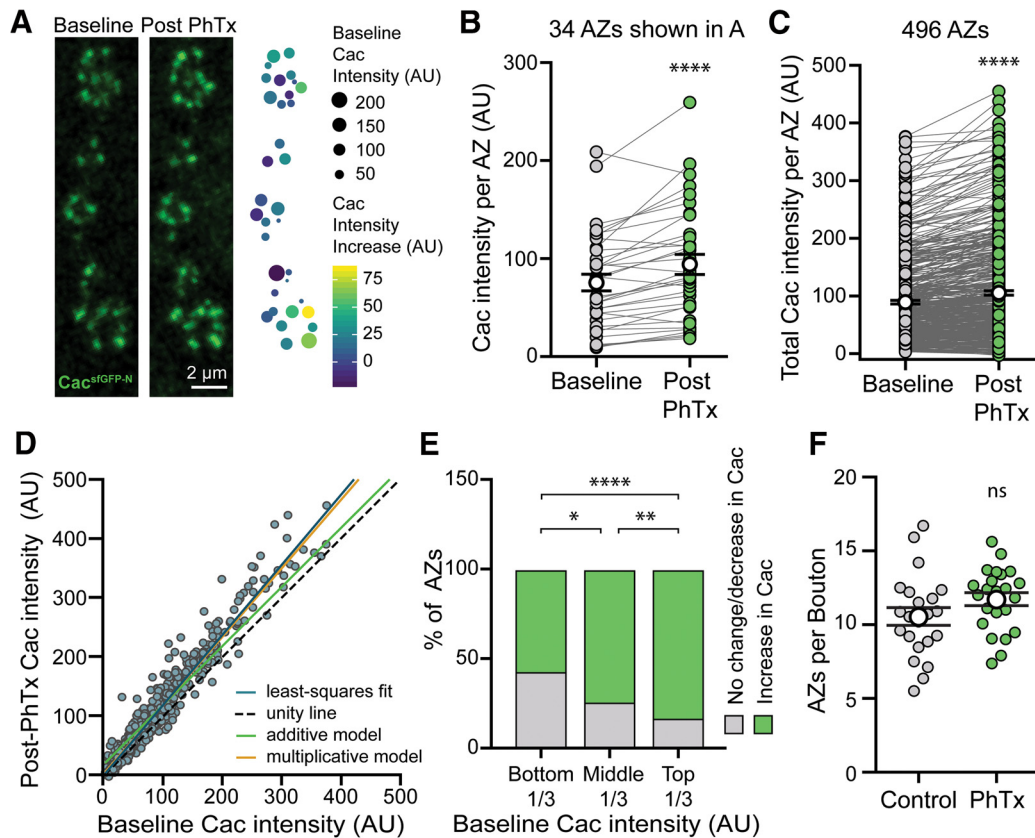
Figure 6. Live imaging of Cac^{sfGFP} reveals Ca^{2+} channel accumulation across heterogeneous AZs during rapid homeostatic adaptation to PhTx application. ***A***, Confocal *Z*-projection of Cac at AZs of a motorneuron branch in a live *cac$^{sfGFP-N}$* preparation immediately before and after 10-min PhTx treatment. The heat map indicates PhTx-induced Cac accumulation (color) relative to baseline Cac levels (size) at each AZ. ***B***, Cac intensity at single AZs of the NMJ shown in ***A*** before and after PhTx reveals Cac accumulation at the majority of AZs (baseline: 75.58 ± 8.55; post-PhTx minus vehicle: 94.25 ± 10.12, *n* = 34 AZs from 1 NMJ branch, *p* < 0.0001, paired *t* test). ***C***, Cac intensity at single AZs across multiple animals also reveals Ca^{2+} channel accumulation at most AZs (Baseline, 89.56 ± 3.24; post-PhTx minus vehicle, 105.7 ± 3.96, *n* = 496 AZs from 7 NMJs and 4 animals, *p* < 0.0001, Wilcoxon signed rank test). ***D***, Cac intensity at individual AZs at baseline versus post-PhTx minus vehicle. The blue line is a least-squares fit to the data (slope = 1.16, R^2 = 0.94), whereas the dotted line would describe the data if there were no effect of PhTx (unity line, slope = 1), the green line would describe the data if there were an additive effect, and the orange line would describe the data if there were a multiplicative effect. ***E***, AZs that experience either no change or a decrease in Ca^{2+} channel content after PhTx occur more frequently in lower Cac-content AZs (bottom-third, 48%; middle-third, 28%; top-third, 13%; bottom vs middle, *p* = 0.003, middle vs top, *p* = 0.02, bottom vs top, *p* < 0.0001, Fisher's exact test). ***F***, AZ number is similar between control and PhTx-treated *cac$^{sfGFP-N}$* NMJs in fixed tissue preparations (control: 10.56 ± 0.60, *n* = 22 NMJs from 6 animals; PhTx: 11.73 ± 0.45, *n* = 23 NMJs from 6 animals, *p* = 0.12, Student's *t* test). Not significant (ns), *p < 0.05, **p < 0.01, and ****p < 0.0001.

found that they were more frequently observed among AZs with lower baseline Cac levels (Fig. 6E). Although imaging constraints make it harder to detect proportional changes in Cac levels at low-content AZs, we observe a significant effect consistent with the conclusion that baseline Cac content influences the likelihood of Ca^{2+} channel accumulation at a particular AZ. Notably, we did not observe significant formation of new AZs in our live preparations, a finding we confirmed in our fixed samples (Fig. 6F). This indicates that potentiation of release occurs largely through the strengthening of existing AZs. Together our findings provide insight into how functional heterogeneity is established at single AZs and further modulated during homeostatic plasticity.

Discussion

Diverse synaptic release properties enable complex communication and may broaden the capacity of circuits to communicate reliably and respond to changing inputs. We have investigated how the regulation of Ca^{2+} channel accumulation at AZs contributes to the establishment and modulation of AZ-specific release properties to maintain stable communication. Endogenous tagging of Cac allowed us to track Ca^{2+} channels live and in fixed

tissue without the potential artifacts associated with transgene overexpression. This approach revealed differences in the regulation of endogenous and exogenous Ca^{2+} channels, underlining the value of developing and validating reagents for following endogenous proteins *in vivo*.

The abundance of endogenous Cac at individual AZs of single motorneurons is heterogeneous and correlates with single-AZ P_r. This is consistent with previous studies in multiple systems linking endogenous Ca^{2+} channel levels at individual AZs to presynaptic release probability and efficacy, and a recent investigation of transgenically expressed Cac (Luo et al., 2011; Holderith et al., 2012; Sheng et al., 2012; Akbergenova et al., 2018). This strong correlation suggests Ca^{2+} channel levels might be regulated to tune P_r during plasticity, so we investigated the modulation of endogenous Cac levels in several *Drosophila* models of presynaptic homeostatic plasticity. Previous studies have suggested that the bidirectional regulation of Ca^{2+} influx at synapses contributes to the modulation of presynaptic release observed during both PHP and PHD (Frank et al., 2006; Müller and Davis, 2012; Müller et al., 2012; Gavino et al., 2015). A long-standing question is whether these changes are achieved through the regulation of channel levels, channel function, or through distinct mecha-

nisms. Multiple mechanisms have been proposed to explain the increase in Ca^{2+} influx observed during the expression of PHP (Frank et al., 2006, 2009; Müller and Davis, 2012; Younger et al., 2013; Brusich et al., 2015; Müller et al., 2015; Kiragasi et al., 2017; Orr et al., 2017). For example, a presynaptic epithelial sodium channel (ENaC) and glutamate autoreceptor (DKaiR1D) have been implicated in promoting Ca^{2+} influx during PHP, leading to the model that modulation of presynaptic membrane potential might increase influx through Cac channels (Younger et al., 2013; Kiragasi et al., 2017; Orr et al., 2017). On the other hand, Frank et al. (2009) found that the guanine exchange factor Ephexin signals through the small GTPase Cdc42 to promote PHP in a Cac-dependent manner, raising the possibility that it does so through actin-dependent accumulation of new channels. Further, multiple AZ cytomatrix proteins, including Fife, RIM, and RIM-binding protein, are necessary to express PHP and also regulate Ca^{2+} channel levels during development (Liu et al., 2011; Bruckner et al., 2012, 2017; Graf et al., 2012; Müller et al., 2012, 2015). However, whether Ca^{2+} channel abundance is modulated during PHP remained an open question.

Here, we demonstrate that Cac abundance is indeed enhanced during both the acute and chronic expression of PHP. This increase occurs in conjunction with the accumulation of Brp and enhancement of the RRP (Weyhersmüller et al., 2011, Goel et al., 2017; Li et al., 2018a), pointing to the coordinated remodeling of the entire neurotransmitter release apparatus during PHP on both timescales. Studies in mammals have found that AZ protein levels are dynamic and subject to homeostatic modification over chronic timescales (Matz et al., 2010; Lazarevic et al., 2011; Spangler et al., 2013; Glebov et al., 2017; Thalhammer et al., 2017), indicating that structural reorganization of AZs is a conserved mechanism for modulating release. As ENaC and DKaiR1D-dependent functional modulation occur in tandem with the structural reorganization of AZs, it is interesting to consider why redundant mechanisms may have evolved. One remarkable feature of PHP is the incredible precision with which quantal content is tuned to offset disruptions to postsynaptic neurotransmitter receptor function. It is therefore tempting to hypothesize that PHP achieves this analog scaling of release probability by simultaneously deploying distinct mechanisms to calibrate the structure and function of AZs.

In contrast to the many mechanisms proposed for modulating Ca^{2+} influx during PHP, far less is known about how Ca^{2+} influx is regulated during PHD. One attractive idea was a reduction in AZ Ca^{2+} channel levels based on studies revealing reduced levels of transgenic UAS-Cac-GFP upon vGlut overexpression (Gavino et al., 2015). However, we found that endogenous Cac channels do not change in conjunction with vGlut overexpression-induced PHD. Because all Cac channels are tagged in *cac*$^{sfGFP-N}$, this observation indicates that a reduction in Cac abundance at AZs is not necessary to achieve PHD. We determined that the source of the discrepancy is the use of the transgene to report overexpressed versus endogenous Cac levels, demonstrating that exogenous and endogenous channels are regulated differently, at least during this form of PHD. This indicates that a mechanism other than modulation of Cac abundance drives PHD expression. Levels of Brp and RRP size are also unchanged during PHD (Gavino et al., 2015; Li et al., 2018a). Thus, the coordinated reorganization of the AZ appears to be specific to PHP. Interestingly, reversible downregulation of a subset of AZ proteins, but not Cac, was observed at *Drosophila* photoreceptor synapses following prolonged light exposure (Sugie et al., 2015). In the future, it will be of interest to determine whether PHP and PHD share any

mechanisms to control the bidirectional modulation of Ca^{2+} influx. PHD signaling operates independently of PHP, and was recently proposed to function as a homeostat responsive to excess glutamate, not synaptic strength, raising the possibility that mechanisms distinct from those that have been elucidated for PHP may regulate presynaptic inhibition during PHD (Li et al., 2018a).

Finally, live imaging of Cac$^{sfGFP-N}$ during acute PHP enabled the investigation of how baseline heterogeneity in Cac levels and P_r intersects with the homeostatic reorganization of AZs. Monitoring endogenous Cac at the same AZs before and after PhTx treatment, we observed the accumulation of Ca^{2+} channels across AZs with diverse baseline properties. As with PHP expression over chronic timescales, our findings leave open the possibility of multiple mechanisms acting simultaneously, perhaps to ensure precise tuning, and do not rule out additional modulation of channel function or indirect regulation of Ca^{2+} influx. In fact, a prevailing model posits rapid events that acutely modulate P_r followed by consolidation of the response for long-term homeostasis (Frank et al., 2006, 2009). Coincident changes in Ca^{2+} channel function and levels coupled with long-term restructuring of AZs provides an attractive mechanism for this model. We also found that Cac accumulation is proportional across low- and high-P_r AZs. Therefore, baseline heterogeneity in Cac levels is maintained following the expression of PHP. At mammalian excitatory synapses, proportional scaling of postsynaptic glutamate receptor levels stabilizes activity while maintaining synaptic weights (Turrigiano, 2012). Our findings suggest an analogous phenomenon could be occurring presynaptically at the *Drosophila* NMJ. Notably, receptor scaling can occur globally or locally (Turrigiano et al., 1998; Yu and Goda, 2009). A recent study reported that PHP can be genetically induced and expressed within individual axon branches (Li et al., 2018b), demonstrating a similar degree of specificity in the expression of PHP at the *Drosophila* NMJ. A proportional increase in Cac levels could arise through homeostatic signaling from individual postsynaptic densities responding to similar decreases in quantal size; a strategy that would allow for both the remarkable synapse specificity and precision with which homeostatic modulation of neurotransmitter release operates.

References

Ackermann F, Waites CL, Garner CC (2015) Presynaptic active zones in invertebrates and vertebrates. EMBO Rep 16:923–938.

Akbergenova Y, Cunningham KL, Zhang YV, Weiss S, Littleton JT (2018) Examining molecular determinants underlying heterogeneity of synaptic release probability using optical quantal imaging. eLife 7:e38268.

Akerboom J, Chen TW, Wardill TJ, Tian L, Marvin JS, Mutlu S, Calderón NC, Esposti F, Borghuis BG, Sun XR, Gordus A, Orger MB, Portugues R, Engert F, Macklin JJ, Filosa A, Aggarwal A, Kerr RA, Takagi R, Kracun S, et al. (2012) Optimization of a GCaMP calcium indicator for neural activity imaging. J Neurosci 32:13819–13840.

Ariel P, Ryan TA (2012) New insights into molecular players involved in neurotransmitter release. Physiology 27:15–24.

Atwood HL, Karunanithi S (2002) Diversification of synaptic strength: presynaptic elements. Nat Rev Neurosci 3:497–516.

Branco T, Staras K (2009) The probability of neurotransmitter release: variability and feedback control at single synapses. Nat Rev Neurosci 10:373–383.

Bruckner JJ, Gratz SJ, Slind JK, Geske RR, Cummings AM, Galindo SE, Donohue LK, O'Connor-Giles KM (2012) Fife, a *Drosophila* piccolo-RIM homolog, promotes active zone organization and neurotransmitter release. J Neurosci 32:17048–17058.

Bruckner JJ, Zhan H, Gratz SJ, Rao M, Ukken F, Zilberg G, O'Connor-Giles KM (2017) Fife organizes synaptic vesicles and calcium channels for high-probability neurotransmitter release. J Cell Biol 216:231–246.

Brusich DJ, Spring AM, Frank CA (2015) A single-cross, RNA interference-based genetic tool for examining the long-term maintenance of homeostatic plasticity. Front Cell Neurosci 9:107.

Cull-Candy SG, Miledi R, Trautmann A, Uchitel OD (1980) On the release of transmitter at normal, myasthenia gravis and myasthenic syndrome affected human end-plates. J Physiol 299:621–638.

Daniels RW, Collins CA, Gelfand MV, Dant J, Brooks ES, Krantz DE, DiAntonio A (2004) Increased expression of the *Drosophila* vesicular glutamate transporter leads to excess glutamate release and a compensatory decrease in quantal content. J Neurosci 24:10466–10474.

Davis GW, Müller M (2015) Homeostatic control of presynaptic neurotransmitter release. Annu Rev Physiol 77:251–270.

Dittrich M, Homan AE, Meriney SD (2018) Presynaptic mechanisms controlling calcium-triggered transmitter release at the neuromuscular junction. Curr Opin Physiol 4:15–24.

Ehmann N, Sauer M, Kittel RJ (2015) Super-resolution microscopy of the synaptic active zone. Front Cell Neurosci 9:7.

Frank CA (2014) Homeostatic plasticity at the *Drosophila* neuromuscular junction. Neuropharmacology 78:63–74.

Frank CA, Kennedy MJ, Goold CP, Marek KW, Davis GW (2006) Mechanisms underlying the rapid induction and sustained expression of synaptic homeostasis. Neuron 52:663–677.

Frank CA, Pielage J, Davis GW (2009) A presynaptic homeostatic signaling system composed of the Eph receptor, ephexin, Cdc42, and CaV2.1 calcium channels. Neuron 61:556–569.

Gavino MA, Ford KJ, Archila S, Davis GW (2015) Homeostatic synaptic depression is achieved through a regulated decrease in presynaptic calcium channel abundance. eLife 4:e05473.

Glebov OO, Jackson RE, Winterflood CM, Owen DM, Barker EA, Doherty P, Ewers H, Burrone J (2017) Nanoscale structural plasticity of the active zone matrix modulates presynaptic function. Cell Rep 18:2715–2728.

Goel P, Li X, Dickman D (2017) Disparate postsynaptic induction mechanisms ultimately converge to drive the retrograde enhancement of presynaptic efficacy. Cell Rep 21:2339–2347.

Graf ER, Daniels RW, Burgess RW, Schwarz TL, DiAntonio A (2009) Rab3 dynamically controls protein composition at active zones. Neuron 64:663–677.

Graf ER, Valakh V, Wright CM, Wu C, Liu Z, Zhang YQ, DiAntonio A (2012) RIM promotes calcium channel accumulation at active zones of the *Drosophila* neuromuscular junction. J Neurosci 32:16586–16596.

Gratz SJ, Ukken FP, Rubinstein CD, Thiede G, Donohue LK, Cummings AM, O'Connor-Giles KM (2014) Highly specific and efficient CRISPR/Cas9-catalyzed homology-directed repair in *Drosophila*. Genetics 196:961–971.

Guerrero G, Reiff DF, Agarwal G, Ball RW, Borst A, Goodman CS, Isacoff EY (2005) Heterogeneity in synaptic transmission along a *Drosophila* larval motor axon. Nat Neurosci 8:1188–1196.

Harris KP, Littleton JT (2015) Transmission, development, and plasticity of synapses. Genetics 201:345–375.

Hatt H, Smith DO (1976) Non-uniform probabilities of quantal release at the crayfish neuromuscular junction. J Physiol 259:395–404.

Holderith N, Lorincz A, Katona G, Rózsa B, Kulik A, Watanabe M, Nusser Z (2012) Release probability of hippocampal glutamatergic terminals scales with the size of the active zone. Nat Neurosci 15:988–997.

Horn C, Offen N, Nystedt S, Häcker U, Wimmer EA (2003) *piggyBac*-based insertional mutagenesis and enhancer detection as a tool for functional insect genomics. Genetics 163:647–661.

Jackman SL, Regehr WG (2017) The mechanisms and functions of synaptic facilitation. Neuron 94:447–464.

Kawasaki F, Felling R, Ordway RW (2000) A temperature-sensitive paralytic mutant defines a primary synaptic calcium channel in *Drosophila*. J Neurosci 20:4885–4889.

Kawasaki F, Collins SC, Ordway RW (2002) Synaptic calcium-channel function in *Drosophila*: analysis and transformation rescue of temperature-sensitive paralytic and lethal mutations of cacophony. J Neurosci 22:5856–5864.

Kawasaki F, Zou B, Xu X, Ordway RW (2004) Active zone localization of presynaptic calcium channels encoded by the cacophony locus of *Drosophila*. J Neurosci 24:282–285.

Kiragasi B, Wondolowski J, Li Y, Dickman DK (2017) A presynaptic glutamate receptor subunit confers robustness to neurotransmission and homeostatic potentiation. Cell Rep 19:2694–2706.

Kittel RJ, Heckmann M (2016) Synaptic vesicle proteins and active zone plasticity. Front Synaptic Neurosci 8:8.

Kittel RJ, Wichmann C, Rasse TM, Fouquet W, Schmidt M, Schmid A, Wagh DA, Pawlu C, Kellner RR, Willig KI, Hell SW, Buchner E, Heckmann M, Sigrist SJ (2006) Bruchpilot promotes active zone assembly, Ca^{2+} channel clustering, and vesicle release. Science 312:1051–1054.

Lazarevic V, Schöne C, Heine M, Gundelfinger ED, Fejtova A (2011) Extensive remodeling of the presynaptic cytomatrix upon homeostatic adaptation to network activity silencing. J Neurosci 31:10189–10200.

Leys C, Ley C, Klein O, Bernard P, Licata L (2013) Detecting outliers: do not use standard deviation around the mean, use absolute deviation around the median. J Exp Soc Psychol 49:764–766.

Li X, Goel P, Wondolowski J, Paluch J, Dickman D (2018a) A glutamate homeostat controls the presynaptic inhibition of neurotransmitter release. Cell Rep 23:1716–1727.

Li X, Goel P, Chen C, Angajala V, Chen X, Dickman DK (2018b) Synapse-specific and compartmentalized expression of presynaptic homeostatic potentiation. eLife 7:e34338.

Littleton JT, Ganetzky B (2000) Ion channels and synaptic organization: analysis of the *Drosophila* genome. Neuron 26:35–43.

Liu KS, Siebert M, Mertel S, Knoche E, Wegener S, Wichmann C, Matkovic T, Muhammad K, Depner H, Mettke C, Bückers J, Hell SW, Müller M, Davis GW, Schmitz D, Sigrist SJ (2011) RIM-binding protein, a central part of the active zone, is essential for neurotransmitter release. Science 334:1565–1569.

Lu Z, Chouhan AK, Borycz JA, Lu Z, Rossano AJ, Brain KL, Zhou Y, Meinertzhagen IA, Macleod GT (2016) High-probability neurotransmitter release sites represent an energy-efficient design. Curr Biol 26:2562–2571.

Luo F, Dittrich M, Stiles JR, Meriney SD (2011) Single-pixel optical fluctuation analysis of calcium channel function in active zones of motor nerve terminals. J Neurosci 31:11268–11281.

Macleod GT (2012) Forward-filling of dextran-conjugated indicators for calcium imaging at the *Drosophila* larval neuromuscular junction. Cold Spring Harb Protoc 2012:791–796.

Macleod GT, Hegström-Wojtowicz M, Charlton MP, Atwood HL (2002) Fast calcium signals in *Drosophila* motor neuron terminals. J Neurophysiol 88:2659–2663.

Macleod GT, Chen L, Karunanithi S, Peloquin JB, Atwood HL, McRory JE, Zamponi GW, Charlton MP (2006) The *Drosophila* cacts2 mutation reduces presynaptic Ca^{2+} entry and defines an important element in Cav2.1 channel inactivation. Eur J Neurosci 23:3230–3244.

Matz J, Gilyan A, Kolar A, McCarvill T, Krueger SR (2010) Rapid structural alterations of the active zone lead to sustained changes in neurotransmitter release. Proc Natl Acad Sci U S A 107:8836–8841.

Melom JE, Akbergenova Y, Gavornik JP, Littleton JT (2013) Spontaneous and evoked release are independently regulated at individual active zones. J Neurosci 33:17253–17263.

Mochida S (2018) Presynaptic calcium channels. Neurosci Res 127:33–44.

Monday HR, Castillo PE (2017) Closing the gap: long-term presynaptic plasticity in brain function and disease. Curr Opin Neurobiol 45:106–112.

Muhammad K, Reddy-Alla S, Driller JH, Schreiner D, Rey U, Böhme MA, Hollmann C, Ramesh N, Depner H, Lützkendorf J, Matkovic T, Götz T, Bergeron DD, Schmoranzer J, Goettfert F, Holt M, Wahl MC, Hell SW, Scheiffele P, Walter AM, et al. (2015) Presynaptic spinophilin tunes neurexin signalling to control active zone architecture and function. Nat Commun 6:8362.

Müller M, Davis GW (2012) Transsynaptic control of presynaptic Ca^{2+} influx achieves homeostatic potentiation of neurotransmitter release. Curr Biol 22:1102–1108.

Müller M, Liu KS, Sigrist SJ, Davis GW (2012) RIM controls homeostatic plasticity through modulation of the readily-releasable vesicle pool. J Neurosci 32:16574–16585.

Müller M, Genc O, Davis GW (2015) RIM-binding protein links synaptic homeostasis to the stabilization and replenishment of high release probability vesicles. Neuron 85:1056–1069.

Nanou E, Catterall WA (2018) Calcium channels, synaptic plasticity, and neuropsychiatric disease. Neuron 98:466–481.

Newman ZL, Hoagland A, Aghi K, Worden K, Levy SL, Son JH, Lee LP, Isacoff EY (2017) Input-specific plasticity and homeostasis at the *Drosophila* larval neuromuscular junction. Neuron 93:1388–1404.e10.

Orr BO, Gorczyca D, Younger MA, Jan LY, Jan YN, Davis GW (2017) Com-

position and control of a Deg/ENaC channel during presynaptic homeostatic plasticity. Cell Rep 20:1855–1866.

Parks AL, Cook KR, Belvin M, Dompe NA, Fawcett R, Huppert K, Tan LR, Winter CG, Bogart KP, Deal JE, Deal-Herr ME, Grant D, Marcinko M, Miyazaki WY, Robertson S, Shaw KJ, Tabios M, Vysotskaia V, Zhao L, Andrade RS, et al. (2004) Systematic generation of high-resolution deletion coverage of the *Drosophila* melanogaster genome. Nat Genet 36:288–292.

Peled ES, Isacoff EY (2011) Optical quantal analysis of synaptic transmission in wild-type and rab3-mutant *Drosophila* motor axons. Nat Neurosci 14:519–526.

Peled ES, Newman ZL, Isacoff EY (2014) Evoked and spontaneous transmission favored by distinct sets of synapses. Curr Biol 24:484–493.

Peng IF, Wu CF (2007) *Drosophila* cacophony channels: a major mediator of neuronal Ca^{2+} currents and a trigger for K+ channel homeostatic regulation. J Neurosci 27:1072–1081.

Petersen SA, Fetter RD, Noordermeer JN, Goodman CS, DiAntonio A (1997) Genetic analysis of glutamate receptors in *Drosophila* reveals a retrograde signal regulating presynaptic transmitter release. Neuron 19:1237–1248.

Reddy-Alla S, Böhme MA, Reynolds E, Beis C, Grasskamp AT, Mampell MM, Maglione M, Jusyte M, Rey U, Babikir H, McCarthy AW, Quentin C, Matkovic T, Bergeron DD, Mushtaq Z, Göttfert F, Owald D, Mielke T, Hell SW, Sigrist SJ, et al. (2017) Stable positioning of Unc13 restricts synaptic vesicle fusion to defined release sites to promote synchronous neurotransmission. Neuron 95:1350–1364 .e12.

Regehr WG (2012) Short-term presynaptic plasticity. Cold Spring Harb Perspect Biol 4:a005702.

Rieckhof GE, Yoshihara M, Guan Z, Littleton JT (2003) Presynaptic N-type calcium channels regulate synaptic growth. J Biol Chem 278:41099-41108.

Schindelin J, Arganda-Carreras I, Frise E, Kaynig V, Longair M, Pietzsch T, Preibisch S, Rueden C, Saalfeld S, Schmid B, Tinevez JY, White DJ, Hartenstein V, Eliceiri K, Tomancak P, Cardona A (2012) Fiji: an open-source platform for biological-image analysis. Nature methods 9:676–682.

Sheng J, He L, Zheng H, Xue L, Luo F, Shin W, Sun T, Kuner T, Yue DT, Wu LG (2012) Calcium-channel number critically influences synaptic strength and plasticity at the active zone. Nat Neurosci 15:998–1006.

Smith LA, Wang X, Peixoto AA, Neumann EK, Hall LM, Hall JC (1996) A *Drosophila* calcium channel α1 subunit gene maps to a genetic locus associated with behavioral and visual defects. J Neurosci 16:7868–7879.

Smith LA, Peixoto AA, Kramer EM, Villella A, Hall JC (1998) Courtship and visual defects of *cacophony* mutants reveal functional complexity of a calcium-channel α1 subunit in *Drosophila*. Genetics 149:1407–1426.

Spangler SA, Schmitz SK, Kevenaar JT, de Graaff E, de Wit H, Demmers J, Toonen RF, Hoogenraad CC (2013) Liprin-α2 promotes the presynaptic recruitment and turnover of RIM1/CASK to facilitate synaptic transmission. J Cell Biol 201:915–928.

Stewart BA, Atwood HL, Renger JJ, Wang J, Wu CF (1994) Improved stability of *Drosophila* larval neuromuscular preparations in haemolymph-like physiological solutions. J Comp Physiol A 175:179–191.

Südhof TC (2012) The presynaptic active zone. Neuron 75:11–25.

Sugie A, Hakeda-Suzuki S, Suzuki E, Silies M, Shimozono M, Möhl C, Suzuki T, Tavosanis G (2015) Molecular remodeling of the presynaptic active zone of *Drosophila* photoreceptors via activity-dependent feedback. Neuron 86:711–725.

Thalhammer A, Contestabile A, Ermolyuk YS, Ng T, Volynski KE, Soong TW, Goda Y, Cingolani LA (2017) Alternative splicing of P/Q-type Ca^{2+} channels shapes presynaptic plasticity. Cell Rep 20:333–343.

Turrigiano G (2012) Homeostatic synaptic plasticity: local and global mechanisms for stabilizing neuronal function. Cold Spring Harb Perspect Biol 4:a005736.

Turrigiano GG, Leslie KR, Desai NS, Rutherford LC, Nelson SB (1998) Activity-dependent scaling of quantal amplitude in neocortical neurons. Nature 391:892–896.

Van Vactor D, Sigrist SJ (2017) Presynaptic morphogenesis, active zone organization and structural plasticity in *Drosophila*. Curr Opin Neurobiol 43:119–129.

Weyhersmüller A, Hallermann S, Wagner N, Eilers J (2011) Rapid active zone remodeling during synaptic plasticity. J Neurosci 31:6041–6052.

Younger MA, Müller M, Tong A, Pym EC, Davis GW (2013) A presynaptic ENaC channel drives homeostatic plasticity. Neuron 79:1183–1196.

Yu LM, Goda Y (2009) Dendritic signalling and homeostatic adaptation. Curr Opin Neurobiol 19:327–335.

Zhan H, Bruckner J, Zhang Z, O'Connor-Giles K (2016) Three-dimensional imaging of *Drosophila* motor synapses reveals ultrastructural organizational patterns. J Neurogenet 30:237–246.